


Designing High-Efficiency Thin Silicon Solar Cells Using Parabolic-Pore Photonic Crystals

Sayak Bhattacharya and Sajeev John*

Department of Physics, University of Toronto, 60 St. George Street, Toronto M5S 1A7, Ontario, Canada

 (Received 23 August 2017; revised manuscript received 19 January 2018; published 6 April 2018)

We demonstrate the efficacy of wave-interference-based light trapping and carrier transport in parabolic-pore photonic-crystal, thin-crystalline silicon (*c*-Si) solar cells to achieve above 29% power conversion efficiencies. Using a rigorous solution of Maxwell's equations through a standard finite-difference time domain scheme, we optimize the design of the vertical-parabolic-pore photonic crystal (PhC) on a 10- μm -thick *c*-Si solar cell to obtain a maximum achievable photocurrent density (MAPD) of 40.6 mA/cm² beyond the ray-optical, Lambertian light-trapping limit. For a slanted-parabolic-pore PhC that breaks *x*-*y* symmetry, improved light trapping occurs due to better coupling into parallel-to-interface refraction modes. We achieve the optimum MAPD of 41.6 mA/cm² for a tilt angle of 10° with respect to the vertical axis of the pores. This MAPD is further improved to 41.72 mA/cm² by introducing a 75-nm SiO₂ antireflective coating on top of the solar cell. We use this MAPD and the associated charge-carrier generation profile as input for a numerical solution of Poisson's equation coupled with semiconductor drift-diffusion equations using a Shockley-Read-Hall and Auger recombination model. Using experimentally achieved surface recombination velocities of 10 cm/s, we identify semiconductor doping profiles that yield power conversion efficiencies over 29%. Practical considerations of additional upper-contact losses suggest efficiencies close to 28%. This improvement beyond the current world record is largely due to an open-circuit voltage approaching 0.8 V enabled by reduced bulk recombination in our thin silicon architecture while maintaining a high short-circuit current through wave-interference-based light trapping.

DOI: [10.1103/PhysRevApplied.9.044009](https://doi.org/10.1103/PhysRevApplied.9.044009)

I. INTRODUCTION

Crystalline silicon (*c*-Si) offers a reliable platform for high-efficiency solar cells [1] owing to the abundance of high-grade Si and the maturity of fabrication techniques. In the absence of nonradiative recombination and assuming perfect solar absorption, the maximum efficiency of a silicon solar cell at room temperature is given by the Shockley-Queisser limit of close to 33% [2]. A recent study by Richter *et al.* puts an upper bound of 29.4% on the conversion efficiency of a single-junction *c*-Si cell by taking into account intrinsic recombination loss in the bulk of the semiconductor [3]. Recently, a record power conversion efficiency of 26.3% was obtained by Kaneka Corporation [4,5] using a 165- μm *c*-Si wafer and a combination of an interdigitated back contact (IBC) and a heterojunction back contact. This cell exhibits an open-circuit voltage (V_{OC}) of 0.744 V. One route to a higher V_{OC} and a higher efficiency is to decrease the Si thickness for reduced bulk recombination when the Si surface is well passivated [6–8]. For example, $V_{\text{OC}} = 0.760$ V was experimentally achieved by Herasimenka *et al.* in a 50- μm -thick *c*-Si single-heterojunction (SHJ) solar cell [7]. However, a thinner Si active layer decreases the optical absorption and short-circuit current density, J_{SC} , unless a different

light-trapping mechanism is used. Photonic-crystal (PhC) [9,10] thin films offer an alternative wave-interference-based light-trapping mechanism. Previous studies have shown that texturing the front surface of the solar cell with modulated nanowires [11], straight and slanted conical nanopores [12], inverted pyramids [13] helps in coupling the incident sunlight to the photonic crystal over the broad wavelength range of the solar AM1.5 global spectrum without much reflection. Phenomena such as parallel-to-interface refraction (PIR) [14] play a pivotal role in significantly improving light absorption over the (800–1100)-nm wavelength range, where a thin *c*-Si active layer would otherwise absorb almost nothing. Optimization studies involving rigorous finite-difference time domain (FDTD) solution of Maxwell's equations have shown that wave-interference-based light trapping can surpass the statistical ray-trapping (Lambertian) limit [15], enabling unprecedented values for the maximum achievable photocurrent density (MAPD) [12]. Out of these different PhC architectures, an inverted-pyramid structure can be mass fabricated conveniently and accurately via low-cost wet-etching techniques [16,17]. However, nonoptimized designs [17] offer a MAPD of 34.5 mA/cm² with a 10- μm -thick Si layer which limits the efficiency to 15.7%. Optimization studies by Eyderman *et al.* [13] have shown that a 10- μm *c*-Si inverted-pyramid structure yields a MAPD (J_{MAPD}) of 42.5 mA/cm². This MAPD is only slightly below the

*john@physics.utoronto.ca

MAPD of 43.5 mA/cm^2 corresponding to perfect absorption of the solar AM1.5 spectrum over a wavelength range of 300–1100 nm. Combining such inverted-pyramid thin films with perovskites to form a tandem solar cell, it is possible to achieve an efficiency over 30% [18].

The underlying physics of wave-interference-based light trapping that distinguishes it from the Lambertian ray-trapping picture consists of two striking physical phenomena. The realization of these effects over the (700–1100)-nm wavelength band requires the fabrication of photonic crystals with specific architectures and wavelength-scale periodicity. The first of these two effects is the deflection of sunlight into directions nearly parallel to the air-silicon boundary, rather than the Lambertian $\cos \theta$ distribution, where θ is the angle of deflection relative to the normal. This parallel-to-interface refraction [14] leads to considerably longer path length augmentation within silicon than the $4n^2$ Lambertian enhancement (where n is the refractive index of the material). This is a wave-interference effect beyond the scope of ray optics. The second physical effect is the slow group velocity of electromagnetic modes in the higher bands of the PhC band structure. Sunlight captured in these slow light modes exhibits a very long dwell time in the material, over and above that suggested by the physical path length enhancement due to the first effect. These two effects combined enable thin films (3–10 μm thick) of silicon to absorb sunlight far beyond the Lambertian limit in the (700–1100)-nm range, and somewhat beyond the Lambertian limit when integration is considered over the entire (300–1100)-nm wavelength range. While the PhC solar-cell architectures we describe in this paper have thicknesses considerably beyond the actual PC depth, these wave-interference effects are clearly seen in a high density of optical resonances (and their electromagnetic-field profiles) over the long wavelength range of the absorption spectrum.

Another architecture exhibiting wave-interference-based solar light trapping for thin *c*-Si solar cells is the parabolic-pore photonic crystal. Unlike the inverted-pyramid structure, this structure is fabricated using reactive-ion etching (RIE) [19]. It was shown previously [19] that this 10- μm -thick tepee-like PhC with a lattice constant of 1200 nm exhibits $J_{\text{MAPD}} = 39.1 \text{ mA/cm}^2$, which is slightly below the Lambertian light-trapping limit (Lambertian absorption yields 39.65 mA/cm^2 for the wavelength range of 300–1100 nm). For a lattice constant of 850 nm, $J_{\text{MAPD}} = 39.7 \text{ mA/cm}^2$, which is slightly above the Lambertian limit.

Our approach to improving solar-cell efficiency remains within the bounds of the Shockley-Queisser limit. However, by surpassing the Lambertian limit for solar absorption and reducing bulk nonradiative Auger recombination through the use of a thin silicon photonic crystal, the so-called practical efficiency limit of 29.4% no longer applies to our designs. A variety of other proposals have been made to surpass the Shockley-Queisser limit itself by absorbing sunlight below the electronic band gap of

silicon. Such proposals involve intermediate band architectures [20,21] or nonlinear optical up-conversion architectures [22]. These approaches increase MAPD beyond 43.5 mA/cm^2 but involve more-complex architectures and typically introduce further issues of nonradiative recombination loss. In this paper, we identify an important and practical way to improve solar-cell efficiency within the Shockley-Queisser bound before looking beyond it.

In this article, we describe how pore optimization and symmetry breaking improve the MAPD toward the perfect absorption limit of 43.5 mA/cm^2 without increasing the *c*-Si active-layer thickness. Our approach enables high J_{SC} and V_{OC} values exceeding 0.75 V, allowing thin-film silicon solar cells to surpass 29% efficiency. For inverted pyramids fabricated by wet etching, for a given lattice constant (a), the height of the pyramids (h) is fixed by the etching angle $\alpha = 54.7^\circ$ between the (111) and (100) planes of a *c*-Si wafer. By contrast, parabolic-pore structures made by RIE allow for the variation of (h/a). The factor (h/a) is an important optimization parameter for light trapping in parabolic-pore PhC solar cells. Specifically, an increasing (h/a) factor results in a more gradual refractive-index variation between air and Si which improves the antireflection of the parabolic-pore PhC. However, increased (h/a) decreases light-absorbing material from the solar cell, leading to an optimal (h/a) factor. Our optimization study shows that for $a = 1000 \text{ nm}$ and (h/a) = 1.7, we obtain the best $J_{\text{MAPD}} = 40.57 \text{ mA/cm}^2$ value for a symmetric parabolic-pore structure. This MAPD exceeds the Lambertian limit as well as the $J_{\text{MAPD}} = 39.7 \text{ mA/cm}^2$ value reported earlier [19]. A significant improvement occurs by breaking the *x*-*y* symmetry of the structure by tilting the parabolic pores. The tilted parabolic-pore PhC provides better light trapping, yielding $J_{\text{MAPD}} = 41.6 \text{ mA/cm}^2$ without antireflective coating (ARC), and $J_{\text{MAPD}} = 41.72 \text{ mA/cm}^2$ with a 75-nm SiO_2 ARC. Our numerical investigation reveals that a slanted parabolic pore couples more energy into PIR modes in the (900–1000)-nm wavelength range than their vertical counterparts. In general, the Lambertian limit is valid for any angle of incidence of incoming sunlight. At normal incidence, our optimized slanted parabolic-pore PhC exceeds the Lambertian limit by approximately 2 mA/cm^2 . Consequently, our optimized cell would exhibit beyond-Lambertian-limit light trapping within a cone of angle 2α , where α is the angle of incidence of the incoming sunlight at which the MAPD of the cell drops by 2 mA/cm^2 compared to the MAPD at normal incidence.

In general, it is time consuming to perform a high-resolution, 3D drift-diffusion calculation for a 10- μm -thick solar cell. For simplicity, we carry out transport calculations for an effective one-dimensional model using an algorithm (described in Sec. II) that uses a spatially averaged generation profile and the MAPD of the 3D FDTD calculation as input to the equivalent one-dimensional solar cell. We benchmark our 1D calculation against the 25%-efficient passivated emitter

and rear locally diffused (PERL) cell [23–25] and verify good agreement between our 1D calculation and experimentally obtained PERL cell current-voltage characteristics. Our numerical results show that it is possible to obtain beyond 29% efficiency with a 10- μm -thick solar cell textured with slanted parabolic pores when the effective surface recombination velocities (SRVs) of the front and rear contacts approach 10 cm/s. Although such low values of SRV have been achieved experimentally for a planar Si wafer with low doping [26], it is challenging to achieve such low SRVs for c -Si with high emitter doping [27]. The 25%-efficient PERL cell [25] has relatively lower emitter doping than that considered in Ref. [27] and, consequently, lower front-surface recombination velocities for electrons (S_n) and holes (S_p). A recent study showed that S_n , S_p , and the trapped charge density of the 25%-efficient PERL cell yield an effective front-surface recombination velocity (SRV_{front}) of 100 cm/s for a donor doping of 10^{18} cm^{-3} [28]. We consider the influence of a higher front SRV on our cell performance in Sec. V. We also optimize the emitter thickness and doping profile, taking into account the power loss in the emitter region due to sheet resistance. Our simulations show that inclusion of such real-world effects allows our 10- μm -thick c -Si cell to reach a conversion efficiency of 28%, still well beyond the current world record.

In this paper, we do not include a detailed consideration of optical shadowing effects of the upper electrical contacts. Roughly speaking, any percentage loss of solar absorption in silicon due to shadowing will lead to a corresponding (multiplicative) percentage loss in efficiency. Experimental measurements in Ref. [29] have shown that a front-contact geometry with a 20- μm finger width and 800- μm finger spacing leads to about a 1% shading loss of J_{SC} . For our proposed cell with the same contact geometry, this shading loss corresponds to an approximately 0.3% (additive) loss of efficiency. However, two recent approaches can be used to recover a major part of this small loss. The first is the use of IBC cells [30–32]. Accurate simulation of an IBC cell would require at least a 2D transport model for photo-generated charge carriers [33]. The second approach is the application of a dielectric coating over the contacts that effectively “cloaks” them by refracting nearly all of the incident sunlight “around” the metal fingers [34–37].

II. SOLAR-CELL ARCHITECTURE AND COMPUTATION DETAILS

We consider two light-trapping geometries: vertical and slanted parabolic-pore PhCs, depicted in Figs. 1(c)–1(g). The PhCs are periodic in the x - y plane, with a lattice constant a along both the x and y directions. The active layer of the solar cell is a c -Si slab of thickness H , backed by a perfect electric conductor (PEC) mirror that prevents light from escaping the solar cell through the rear surface. The PEC layer has a thickness $t_{\text{PEC}} = 100 \text{ nm}$. A SiO_2 buffer layer,

with thickness t_{buffer} and refractive index n_{buffer} , placed between the backreflector and the c -Si slab acts as rear passivation. As we describe in Sec. III, a glass buffer layer with $t_{\text{buffer}} = 75 \text{ nm}$ also provides a slight enhancement in light trapping. The vertical parabolic pores at the front surface of the c -Si slab have a depth h [shown in Fig. 1(d)].

A cross-section view of the PhC-based solar cell is shown in Fig. 1(a). The emitter of the solar cell is a very thin, conformal (width $t_{\text{emitter}} = 100 \text{ nm}$) n -type region with a doping density N_d , and the base region is p type with a doping density N_a . The PEC at the rear surface of the cell makes contact with the active layer through highly p -doped (p^+) back-surface-field (BSF) regions and serves as the rear contact to the solar cell. Similarly, an insulating layer of SiO_x or SiN_x [38,39] at the front surface of the cell acts as front passivation. The shape of the passivation layer influences the optical performance of the cell since it also acts as ARC for incoming sunlight. We consider both conformal [Fig. 1(f)] and nonconformal [Fig. 1(g)] models of the front ARC layer in our optical calculations. In the case of conformal geometry, t_{ARC} denotes the thickness normal to the parabolic shape, whereas, in the nonconformal case, t_{ARC} denotes the vertical height of the ARC. The front electrodes can be made of either indium tin oxide or metal which makes contact with the PhC through highly n -doped (n^+) regions. In order to provide a concrete model of sheet resistance, the spacing between the front-contact fingers can be assumed to be roughly 800 μm , with a 20- μm finger width. This configuration is the same as that used in a 25%-efficient PERL cell [23].

In order to break the x - y symmetry, the vertical parabola is rotated counterclockwise by an angle θ about the y axis. In the rotated coordinate system defined by $x' = x \cos \theta - z \sin \theta$ and $z' = x \sin \theta + z \cos \theta$, the slanted parabola is defined by $z' = kx'^2$, where k is determined from the (h/a) value of the pores. The solution of this quadratic equation defines the slanted parabolic profile in the original coordinate system.

$\theta = 0^\circ$ corresponds to the vertical parabolic-pore case. In our FDTD calculation, we vary θ over a range of 0° – 15° to study the effect of x - y symmetry breaking on the light-trapping capability of PhCs. The cross-section view of the slanted parabolic pore is shown in Fig. 1(e).

Our 3D FDTD calculations are performed using the open-source Electromagnetic Template Library (EMTL) [40]. A periodic boundary condition is applied along the x and y directions, and perfectly matched layers are placed at the computation boundaries normal to the z direction. The solar cell is illuminated by a normally incident broadband plane wave that contains significant energy in the wavelength range of 300–1100 nm. The reflection (R) and transmission (T) are measured by placing two flux planes: one between the cell and the computation box boundary at the top, and the other one between the PEC and the computation box boundary at the bottom. Since there is no absorption in the PEC, the total

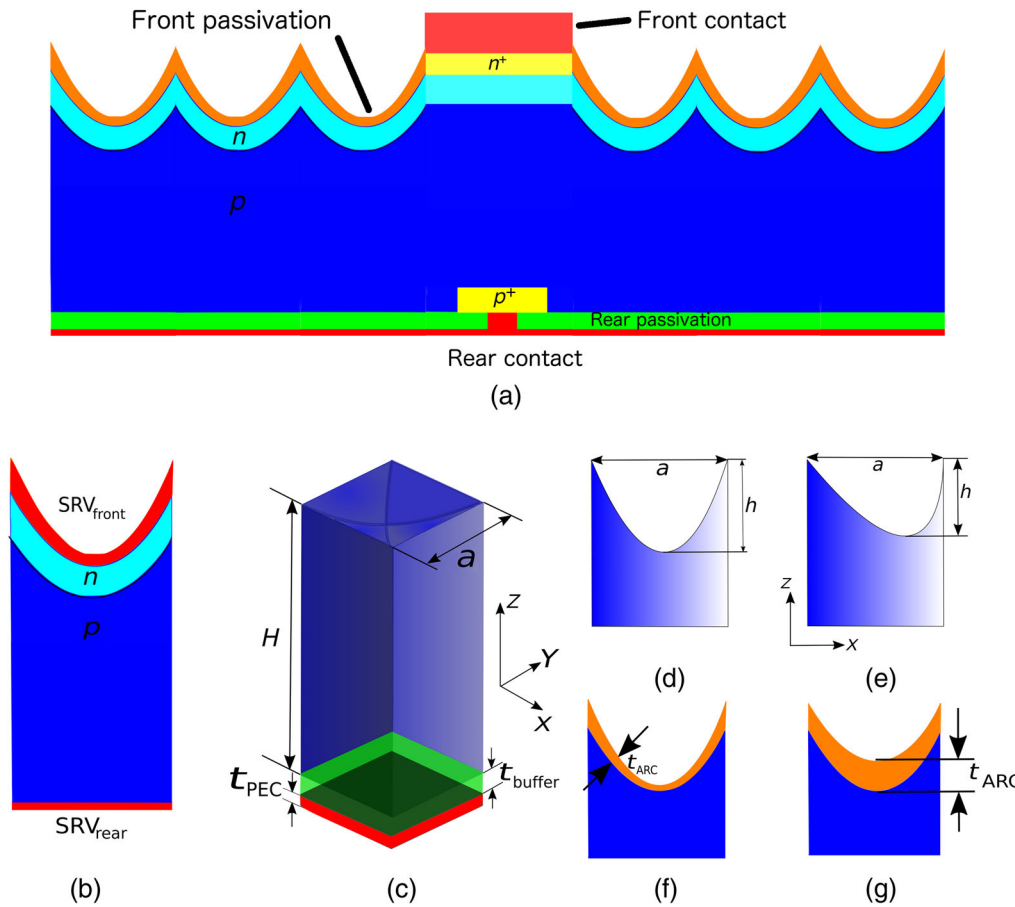


FIG. 1. Parabolic-pore PhC solar-cell architecture. (a) Cross-section view of the 3D cell (not to scale). (b) Model used for carrier transport calculations. The details of the contact and passivation geometries, the effect of passivation, the BSF, etc., are accounted for by SRV_{front} and SRV_{rear} . (c) Unit cell of the parabolic-pore PhC. The buffer layer and the PEC back-reflector are shown as green and red slabs, respectively. x - z views of the (d) vertical and (e) slanted parabolic pores. y - z views of both architectures are the same as in (d). (f) Conformal and (g) nonconformal ARC layers.

absorption $A(\lambda)$ in the active layer of the solar cell is given by $A(\lambda) = 1 - R(\lambda) - T(\lambda)$.

The number of photons absorbed by the solar cell at a given wavelength λ can be found by multiplying the number of incident photons by $A(\lambda)$. The total number of incident photons at a wavelength λ is given by $\lambda I(\lambda)/hc$, where $I(\lambda)$ is the intensity of the incident AM1.5 global spectrum, h is Planck's constant, and c is the speed of light in vacuum. We assume that each of these absorbed photons produces one electron-hole pair. The MAPD represents the short-circuit current produced by the solar cell when all of the generated carriers are collected at the electrodes without any loss. Thus, the MAPD generated over a wavelength range of 300–1100 nm is given by

$$J_{\text{MAPD}} = \int_{\lambda=300\text{nm}}^{\lambda=1100\text{nm}} \frac{e\lambda}{hc} I(\lambda) A(\lambda) d\lambda. \quad (1)$$

In order to evaluate the electronic performance of our proposed solar cell, carrier drift-diffusion equations are numerically solved using the open-source software package Microvolt [41]. To avoid a time-consuming 3D transport calculation, we use an equivalent 1D model in Microvolt that accurately recaptures the current density–voltage (J - V) characteristics of the actual 3D solar cell. The thickness of the c -Si layer in the 1D model is kept the same as that of the

3D cell. The detailed geometries of the contacts, passivation layers, and the BSF are subsumed into effective values for the surface recombination velocities of the front and rear contacts of the equivalent 1D cell. These SRVs enter the computation as boundary conditions for the drift-diffusion equations. A 1D generation profile can be obtained by integrating the actual 3D generation profile obtained by EMTL in the x and y directions within a unit. We find, however, that the precise details of the generation profile have a nearly negligible influence on the resulting J - V characteristics. Accordingly, we use a simplified 1D generation profile that imparts different Beer-Lambert absorption profiles for each wavelength according to the wavelength-dependent decay constants $\alpha(\lambda) = 4\pi k(\lambda)/\lambda$, where $k(\lambda)$ is the imaginary part of the refractive index of c -Si [42].

The equivalent 1D generation profile for our 3D solar cell is determined by a two-step procedure. First, we set the diffusion length very large compared to the cell thickness and set the front and rear SRVs very small (in order to ensure negligible recombination both in the bulk and at the surface). We define the short-circuit current produced by the 1D cell (in the absence of any recombination loss) as J_{SC0} . We then scale up the overall generation profile such that $J_{\text{SC0}} \rightarrow J_{\text{MAPD}}$ of our 3D solar cell.

In order to verify the accuracy of our algorithm, we use our 1D transport calculation to reproduce the V_{OC} , the J_{SC} ,

the conversion efficiency (η), and the fill factor (FF) of the 25%-efficient PERL cell [23–25]. The doping-dependent mobilities of the electrons and holes are implemented using the model of Masetti *et al.* [43]. In our computation, we consider two different models of bulk recombination. It has been shown that hydrogenation of Czochralski-grown *c*-Si wafers can increase bulk minority-carrier lifetimes substantially by passivating the bulk defect states [44]. Further experimental studies in Refs. [45–47] showed that it is possible to achieve lifetimes exceeding the intrinsic Auger limit. Consequently, in the first model, we choose the diffusion lengths, L_n and L_p , of the electrons and holes somewhat independently of the doping concentrations. For a particular doping level, the mobility of the carriers is set by the Masetti *et al.* model [43], and the diffusivities, D_n and D_p , of the electrons and holes are calculated from Einstein's relation. For a given L_n (or L_p), the effective bulk lifetime τ_{neff} (or τ_{peff}) is given by $\tau_{\text{neff}} = L_n^2/D_n$.

In the second model, we take into account Auger recombination, which fixes the diffusion length for a given doping. In this case, we calculate the Auger lifetime (τ_{Aug}) using the model of Kerr and Cuevas [48]. The Shockley-Read-Hall (SRH) recombination is accounted for by assuming the SRH lifetime, $\tau_{\text{SRH}} = 1.2$ ms. We then calculate the effective bulk lifetime τ_{eff} from the following relation:

$$\frac{1}{\tau_{\text{eff}}} = \frac{1}{\tau_{\text{SRH}}} + \frac{1}{\tau_{\text{Aug}}}. \quad (2)$$

Using these input parameters, the semiconductor drift-diffusion equations are numerically solved for various doping levels, diffusion lengths (bulk lifetimes), and effective front and rear SRVs to obtain the J - V characteristics of the solar cell. From the J - V characteristics, we obtain J_{SC} , V_{OC} , the FF, and the power conversion efficiency:

$$\eta = \text{FF} \frac{J_{\text{SC}} V_{\text{OC}}}{P_{\text{inc}}}. \quad (3)$$

Here, $P_{\text{inc}} = 1000$ w/m² is the incident power of the AM1.5 global spectrum.

III. LIGHT-TRAPPING OPTIMIZATION

Wave-interference-based light trapping plays an essential role in enabling a next-generation thin-film silicon solar cell to absorb as much as conventional counterparts that are 10–50 times thicker. PhC-based optical resonances provide an effective way to increase the lifetime of near-infrared photons in the active layer. We now present the results of our light-trapping optimization studies for both vertical and slanted parabolic-pore PhCs. In the case of the vertical parabolic-pore PhC, we vary the height (h) of the pores for

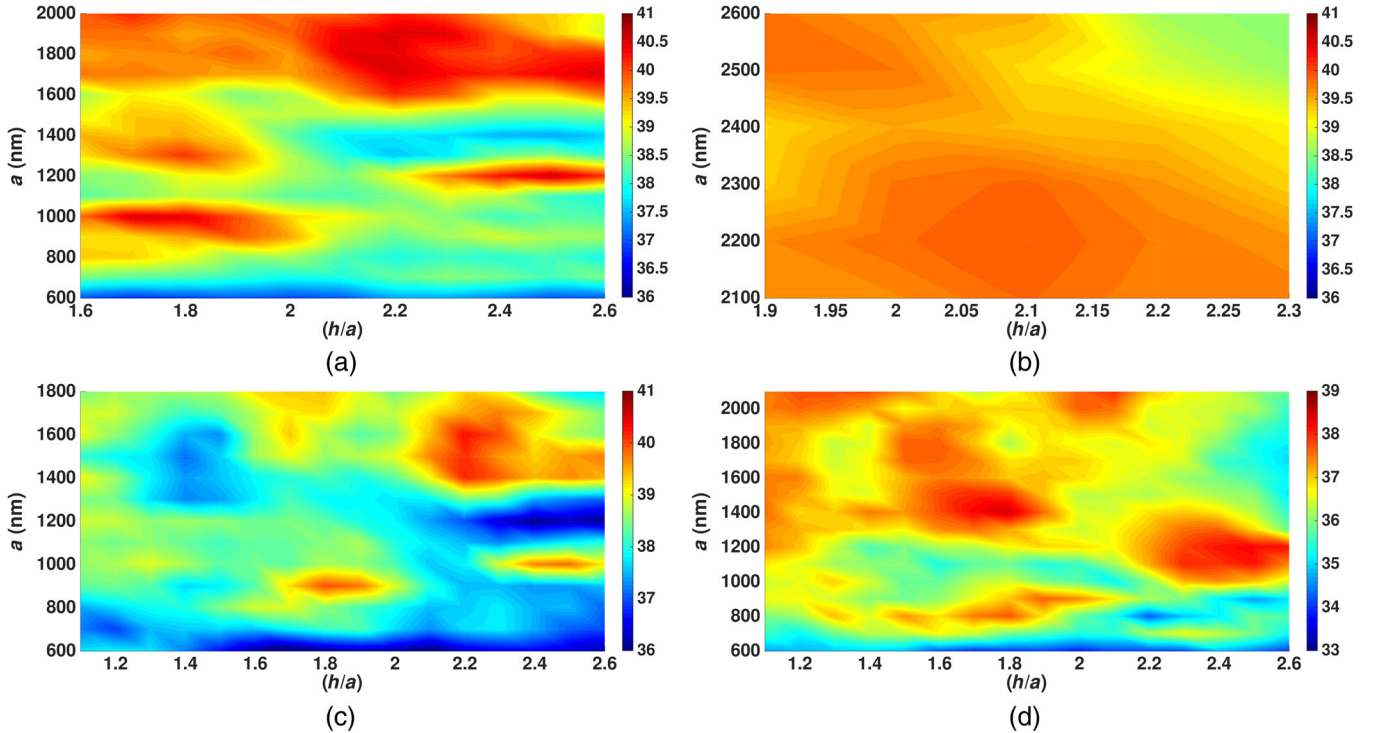


FIG. 2. Optimization map for the MAPD in a vertical parabolic-pore PhC: (a),(b) $H = 10$ μm , (c) $H = 8$ μm , and (d) $H = 5$ μm . For each of these cases, $t_{\text{PEC}} = 100$ nm, $t_{\text{buffer}} = 75$ nm, and $t_{\text{ARC}} = 0$. For $H = 10$ μm , the optimum MAPD of 40.57 mA/cm² is obtained for $a = 1000$ nm and $(h/a) = 1.8$. For $H = 8$ μm , the optimum MAPD value is 40.29 mA/cm² for $a = 1800$ nm and $(h/a) = 2.2$. However, obtaining $(h/a) = 2.2$ can be difficult from a fabrication point of view. Thus, $a = 900$ nm and $(h/a) = 1.8$, with the MAPD 39.98 mA/cm² can be chosen as the optimum point in (c). For $H = 5$ μm , the optimum point is $a = 1400$ nm and $(h/a) = 1.8$, with the MAPD 38.48 mA/cm².

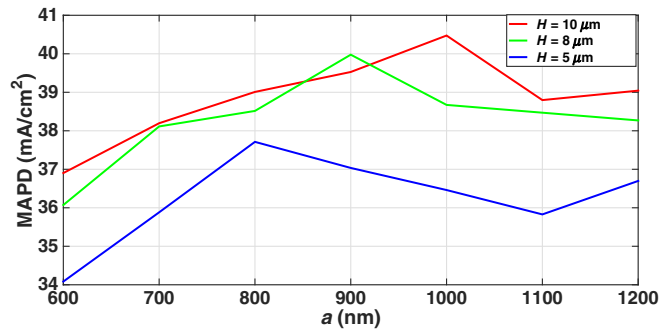


FIG. 3. Existence of a robust ratio $(h/a) = 1.8$. This ratio exhibits local maxima in the optimization map in the range $800 \leq a \leq 1000$ nm for $H = 5, 8,$ and $10 \mu\text{m}$. As we decrease the active-layer thickness, the peak shifts from a higher lattice constant to a lower lattice constant.

different values of a . In a RIE setup, this variation can be achieved by varying the etching power. The parabolic-pore PhC combines the advantages of parallel-to-interface refraction and light-trapping multiple coherent scattering events in the x - y plane and suppressed reflection enabled by the gradual profile variation in the z direction. As we increase (h/a) , the parabolic pore presents a more gradual antireflective profile, but as more Si is etched away, the photogeneration volume is decreased. These two competing effects define an optimum (h/a) for a given a .

Figure 2(a) shows the MAPD optimization map for a vertical parabolic-pore PhC solar cell with $H = 10 \mu\text{m}$, $t_{\text{buffer}} = 75$ nm, and $n_{\text{buffer}} = 1.5$. An optimum MAPD of 40.57 mA/cm^2 is achieved for $a = 1000$ nm and $(h/a) = 1.7$. There are a few more hot spots in the optimization map which offer MAPDs beyond 40.00 mA/cm^2 : $a = 1300$ nm and $(h/a) = 1.8$, with $\text{MAPD} = 40.1 \text{ mA/cm}^2$; $a = 1800$ nm and $(h/a) = 2.1$, with $\text{MAPD} = 40.45 \text{ mA/cm}^2$; $a = 1700$ nm and $(h/a) = 2.2$, with $\text{MAPD} = 40.51 \text{ mA/cm}^2$; and $a = 1200$ nm and $(h/a) = 2.5$, with $\text{MAPD} = 40.53 \text{ mA/cm}^2$. The last three hot spots offer MAPDs which are very close to our optimum point. However, shallower pores are easier to etch and lead to a more robust structure, so we focus attention on $a = 1000$ nm and $(h/a) = 1.7$. We note that the optimum (h/a) shifts higher for larger lattice constants. The corresponding optimization map for $a > 2000$ nm is shown in Fig. 2(b). For $a = 2200$ nm and $(h/a) = 2.1$, we find a weaker local maxima with $\text{MAPD} = 39.9 \text{ mA/cm}^2$. Clearly, the optimization of parabolic-pore PhC is different from that of the inverted-pyramid PhC [13]. The $10\text{-}\mu\text{m}$ -thick inverted-pyramid PhC solar cell has its optimum MAPD at $a = 2500$ nm, whereas the $10\text{-}\mu\text{m}$ -thick parabolic-pore PhC solar cell has its best solar absorption at $a = 1000$ nm.

Figures 2(c) and 2(d) show the optimization maps for thinner silicon films of $H = 8 \mu\text{m}$ and $H = 5 \mu\text{m}$, respectively. For $H = 8 \mu\text{m}$, we find three local maxima offering substantial MAPDs: $a = 1600$ nm and $(h/a) = 2.2$, with

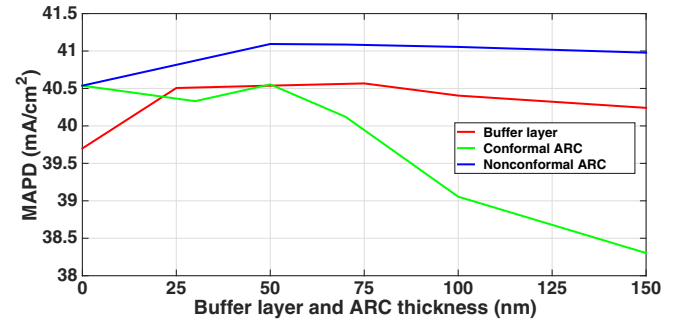


FIG. 4. Optimization of buffer-layer thickness (t_{buffer}) and ARC thickness (t_{ARC}). The optimized values of t_{buffer} and t_{ARC} (non-conformal) are 75 and 50 nm, respectively. Also, note that nonconformal ARC performs better than the conformal geometry.

$\text{MAPD} = 40.29 \text{ mA/cm}^2$; $a = 1000$ nm and $(h/a) = 2.5$, with $\text{MAPD} = 39.83 \text{ mA/cm}^2$; and $a = 900$ nm and $(h/a) = 1.8$, with $\text{MAPD} = 39.98 \text{ mA/cm}^2$. For $H = 5 \mu\text{m}$ the hot spots are located at $a = 1400$ nm and $(h/a) = 1.8$, with $\text{MAPD} = 38.48 \text{ mA/cm}^2$; $a = 1200$ nm and $(h/a) = 2.5$, with $\text{MAPD} = 38.2 \text{ mA/cm}^2$; and $a = 800$ nm and $(h/a) = 1.8$, with $\text{MAPD} = 37.71 \text{ mA/cm}^2$. Out of the hot spots in the optimization maps of Fig. 2, one particular extremum exhibits interesting characteristics. If we scan through the optimization maps keeping (h/a) fixed at 1.8, we see that there is always a maxima near $a = 800$ – 1000 nm, irrespective of H . These peaks corresponding to $(h/a) = 1.8$ are shown in Fig. 3. As H is decreased, the peak shifts toward lower a values. Thus, the factor $(h/a) = 1.8$ is a robust ratio with respect to the thickness variation of the solar cell. Also, a comparison of the hot spots in the optimization maps suggests that the maxima corresponding to this ratio is narrower with respect to variation of the lattice constant compared to other hot spots, which appear to be broader. Broader maxima suggest a considerable robustness to disorder effects.

While the buffer layer provides rear passivation to the solar cell, it can also improve light trapping (see Fig. 4). In absence of the buffer layer the MAPD of the solar cell is only

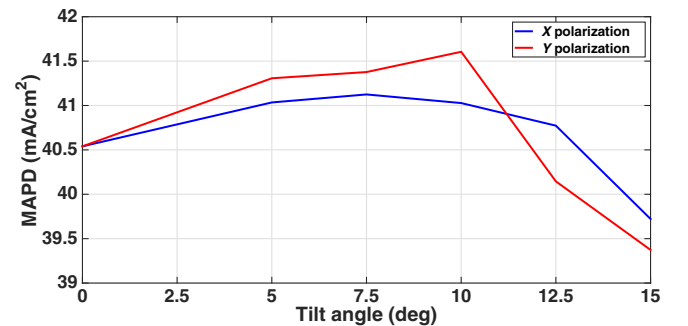


FIG. 5. Variation of the MAPD of a slanted parabolic pore with tilt angle θ for excitations polarized along the x and y directions. The improvement for y -polarized light is greater when the pores are tilted along the x axis [shown in Fig. 1(e)].

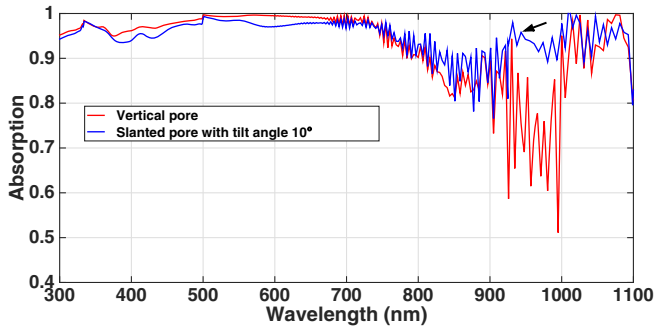


FIG. 6. Comparison of absorption spectra under y -polarized excitation for an x - y -symmetric (vertical parabolic-pore) structure and x - y -symmetry-breaking (slanted parabolic-pore) structures. For both cases, $t_{\text{buffer}} = 75$ nm, $t_{\text{ARC}} = 0$, and $t_{\text{PEC}} = 100$ nm. The symmetry-breaking PhC absorbs more light in the (750–1010)-nm wavelength range.

39.7 mA/cm² for $a = 1000$ nm and $h = 1700$ nm. By introducing a 25-nm-thick buffer of glass ($n_{\text{buffer}} = 1.5$), the MAPD improves by 0.8 mA/cm² to 40.51 mA/cm². The optimum value of t_{buffer} is 75 nm, providing the previously quoted MAPD of 40.57 mA/cm². Furthermore, we investigate the effect of the front passivation layer or the ARC on the optical performance of the solar cell. Figure 4 suggests that a nonconformal ARC layer is better than a conformal ARC, as the former improves the MAPD by 0.5 mA/cm² for an optimum thickness of 50 nm, whereas the conformal ARC does not improve the MAPD. Overall, for

$a = 1000$ nm, $h = 1700$ nm, $t_{\text{buffer}} = 75$ nm, and a non-conformal ARC of thickness 50 nm, we obtain the optimum MAPD of 41.09 mA/cm² for a 10 - μm thick solar cell textured with a vertical parabolic-pore PhC.

An improvement to the MAPD is realized if we break the x - y symmetry of the structure by tilting the pores along the x direction according to the method outlined in Sec. II. We keep the lattice constant fixed at 1000 nm and (h/a) at 1.7 , and the tilt angle θ is varied over a range of 0° – 15° . We excite the structure separately with x - and y -polarized plane waves in order to study the polarization response of the structure. The MAPD values corresponding to different tilt angles are shown in Fig. 5 for both polarizations. Without any ARC layer, we obtain the optimum MAPD of 41.6 mA/cm² for the y -polarized case at $\theta = 10^\circ$, which shows an improvement of approximately 1 mA/cm² from the x - y -symmetric case. For an x -polarized incident wave, the optimum MAPD is 41.1 mA/cm² at $\theta = 7.5^\circ$, an improvement of about 0.5 mA/cm² from the symmetric case. For $\theta = 10^\circ$, the MAPD corresponding to x -polarized incident radiation is 41.05 mA/cm² and, for $\theta = 7.5^\circ$, the MAPD corresponding to the y -polarized excitation is 41.35 mA/cm². Thus, on average, we find a slightly higher overall MAPD for the $\theta = 10^\circ$ than for the $\theta = 7.5^\circ$ case.

To understand the underlying cause of the significant MAPD improvement for y -polarized light, we compare the absorption spectra of the vertical and slanted parabolic pores in Fig. 6. Clearly, the slanted pore absorbs more

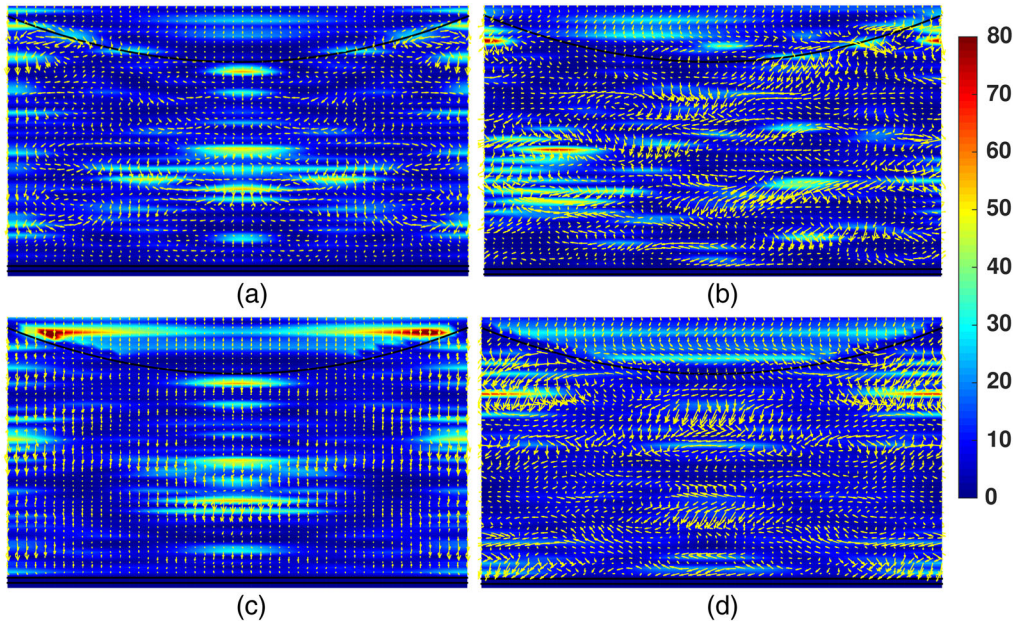


FIG. 7. Plot of the energy density and the in-plane Poynting vector for vertical and slanted-pore PhCs at $\lambda = 940$ nm. The incident plane wave is polarized along the y direction. The x - z slice (passing through the center of the unit cell) for the (a) vertical and (b) slanted pores. The Poynting vectors show significant parallel-to-interface power flow and prominent formation of vortices in (b) compared to (a). The central y - z slice for the (c) vertical and (d) slanted pores. For the vertical pores, almost all of the power flows from top to bottom. However, (d) shows prominent vortices in the power flow pattern and the parallel-to-interface Poynting vectors. Clearly, PIR into slow-light modes is a key mechanism for better light trapping in the x - y symmetry-broken structure.

sunlight in the (750–1010)-nm wavelength range. The arrow in Fig. 6 points to a 95.6% absorption peak at $\lambda = 940$ nm for the slanted parabolic PhC, compared to only 77.2% for its vertical counterpart. In Fig. 7, we plot the energy density distributions and in-plane components of the Poynting vectors along orthogonal slices for y -polarized excitation. The energy densities are normalized by the incident energy density. Figures 7(a) and 7(b) correspond to the x - z -plane data slices, and Figs. 7(c) and 7(d) correspond to y - z slices for the vertical and slanted pore PhCs, respectively. Figure 7(a) shows a small amount of energy flow parallel to the interface, and some vortexlike paths near the intensity peaks. In Fig. 7(b), both parallel-to-interface energy flow and vorticity near the hot spots are significantly more prominent. The same conclusion applies to the y - z -plane energy flows shown in Figs. 7(c) and 7(d). In the case of the x - y -symmetric PhC, the energy flows predominantly along the z direction, but when we break the x - y symmetry, the Poynting vector exhibits considerable parallel-to-interface energy flow. The resulting long dwell time of photons within the active layer ensures strong absorption.

IV. CARRIER TRANSPORT AND SOLAR-CELL PERFORMANCE

We begin by benchmarking our approximate 1D transport model against the well-known 25%-efficient PERL cell

[23–25]. This cell employs a passivation layer between the backreflector and the active layer. The rear metal contacts the active layer only through highly doped p regions that provide a BSF. A similar strategy applies to the front contacts. The overall effect of surface passivation (both chemical and trapped charge) in the 3D PERL cell is accounted for in our 1D model by effective SRVs at the top and bottom of the solar cell. Robinson *et al.* numerically investigated a 2D model of the PERL cell [25]. They considered a band-gap-narrowing effect that increased the MAPD of the cell and perimeter recombination [49] that involved adjustment of V_{OC} by 6 mV above the measured value. In our 1D model, these effects are not considered; instead, the SRVs are chosen to best fit the performance parameters (J_{SC} , V_{OC} , the FF, and η) of the PERL cell. We model the 400- μ m-thick PERL cell using an equivalent 1D cell of the same thickness with a Gaussian doping profile for the 1- μ m-thick n -type emitter (the same as the experimentally measured profile [25]). The Gaussian doping profile for the emitter has a peak value of $5 \times 10^{18} \text{ cm}^{-3}$ and drops to $1.41 \times 10^{16} \text{ cm}^{-3}$ at the junction. The thick p -type base region is modeled as a 399- μ m-thick uniformly doped region with $N_a = 1.41 \times 10^{16} \text{ cm}^{-3}$. For carrier recombination, we set $\tau_{SRH} = 1 \text{ ms}$ [25]. The Auger lifetime and effective bulk lifetime of the carriers are modeled according to Eq. (2).

The PERL cell exhibits $J_{SC} = 42.7 \text{ mA/cm}^2$, suggesting that band-gap narrowing effects expand the solar

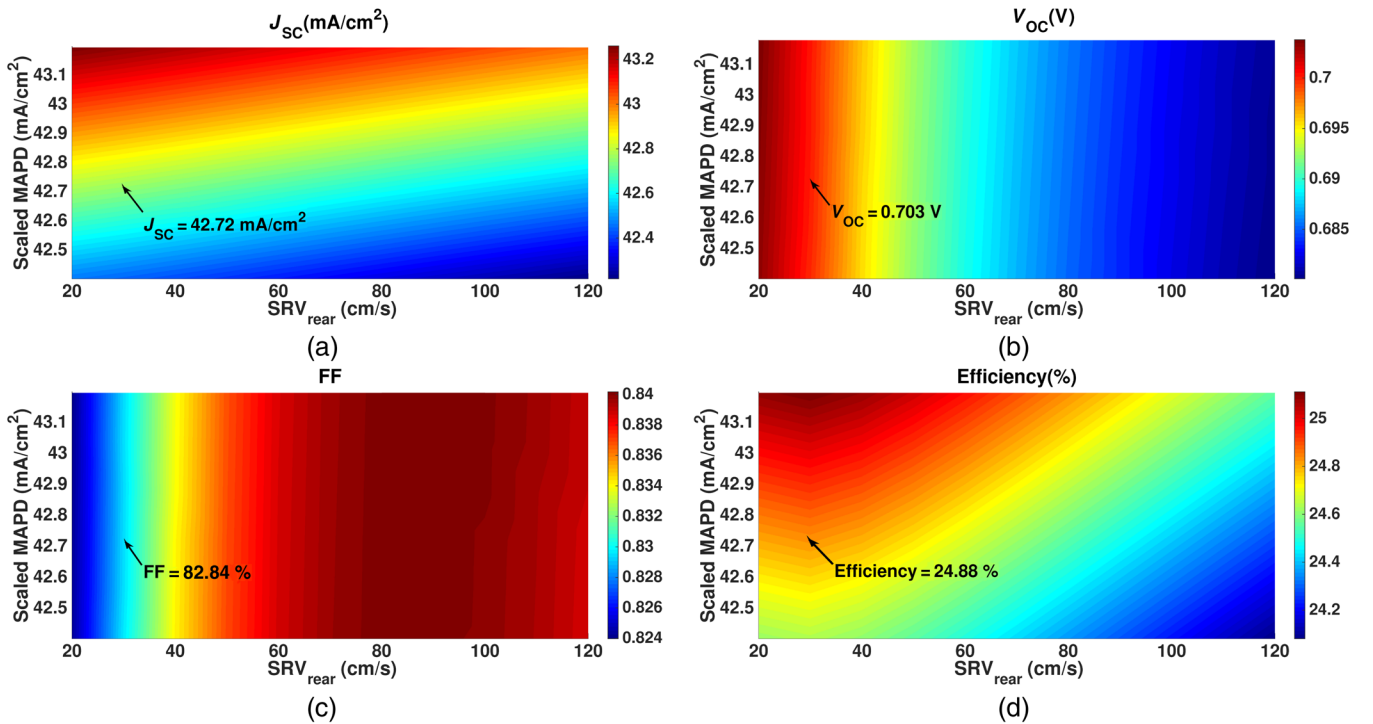


FIG. 8. Validation of a 1D transport model against 25%-efficient PERL cell performance parameters. The scaled MAPD for the generation profile (described in Sec. II) and SRV_{rear} are treated as independent variables. (a)–(d) Color maps for J_{SC} , V_{OC} , the FF, and η , respectively. The 1D model can accurately capture all of the experimentally measured PERL cell performance parameters for a unique choice of scaled MAPD = 42.76 mA/cm² and $SRV_{rear} = 30 \text{ cm/s}$.

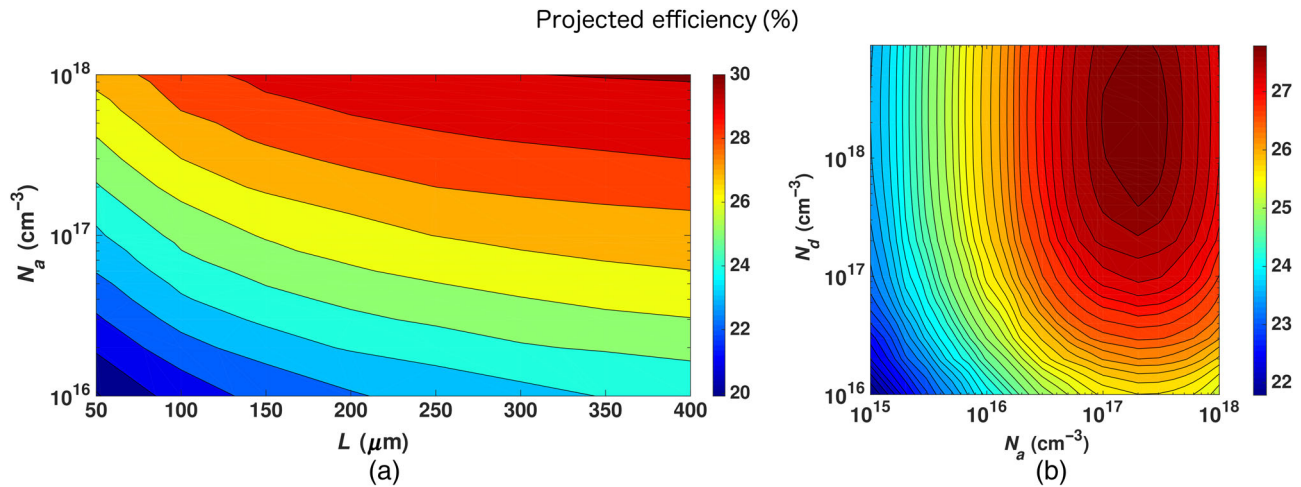


FIG. 9. Contour plots of efficiency for (a) doping-independent diffusion length and (b) doping-dependent lifetime and diffusion length due to Auger recombination. The p - n junction is assumed to be located 100 nm below the top passivation-layer-Si interface. In (a), N_d is kept fixed at 10^{18} cm^{-3} . Near 30% efficiency is obtained for $N_a = 1 \times 10^{18}$ and $L = 300 \mu\text{m}$. (b) shows that Auger recombination reduces the optimum efficiency to 27.9%, achieved for $N_d = 2 \times 10^{18} \text{ cm}^{-3}$ and $N_a = 2 \times 10^{17} \text{ cm}^{-3}$. In both cases, we set $\text{SRV}_{\text{front}} = \text{SRV}_{\text{rear}} = 10 \text{ cm/s}$.

absorption spectrum to wavelengths slightly larger than 1100 nm. In principle, it is possible to estimate the extent of band-gap narrowing (BGN) from knowledge of the detailed doping profile of the PERL cell. However, our aim is to show that our 1D model can accurately capture the experimental performance parameters of an actual 3D cell through boundary conditions imposed by an effective $\text{SRV}_{\text{front}}$ and SRV_{rear} that subsumes the effect of BGN. We recapture the experimental J_{SC} (which already involves BGN) of the PERL cell through the scaling parameter discussed in Sec. II. The other physical manifestation of BGN is a slight drop in the V_{OC} of the cell. An increase in the SRV recaptures this drop in V_{OC} , while maintaining J_{SC} at a constant value (Fig. 10). In this way, our equivalent $\text{SRV}_{\text{front}}$ and SRV_{rear} values simulate the effect of BGN. Accordingly, in our 1D model, we rescale the MAPD along with $\text{SRV}_{\text{front}}$ and SRV_{rear} in order to recapture the observed characteristics of the PERL cell. Variation in $\text{SRV}_{\text{front}}$ over the range of 1–200 cm/s has little effect on the cell performance, so we set $\text{SRV}_{\text{front}} = 140 \text{ cm/s}$ and vary the MAPD scale factor and SRV_{rear} to recapture the PERL cell performance parameters. The results for J_{SC} , V_{OC} , the FF, and η are shown in Fig. 8. The plots reveal a unique choice of scale factor and SRV_{rear} , for which we can reproduce the experimentally obtained J - V characteristics. For $\text{MAPD} = 42.76 \text{ mA/cm}^2$ and $\text{SRV}_{\text{rear}} = 30 \text{ cm/s}$, we obtain $J_{\text{SC}} = 42.72 \text{ mA/cm}^2$, $V_{\text{OC}} = 0.703 \text{ V}$, $\text{FF} = 82.84\%$, and $\eta = 24.88\%$, compared to the experimentally measured values of 42.7 mA/cm^2 , 0.706 V , $\text{FF} = 82.8\%$, and $\eta = 24.96\%$. This calculation suggests a unique mapping of reasonable accuracy between real 3D solar cells and our 1D transport model, given appropriate choices of the MAPD, the SRVs, and τ_{eff} .

We now consider our best 10- μm -thick slanted-pore solar cell exhibiting MAPD of 41.72 mA/cm^2 . In our transport

calculations, we consider a 100-nm-thick uniformly doped n -type emitter region with $N_d = 1 \times 10^{18} \text{ cm}^{-3}$. Before considering the important Auger recombination model, we vary the carrier diffusion lengths independently of doping and set $L_n = L_p \equiv L$. Both $\text{SRV}_{\text{front}}$ and SRV_{rear} are fixed to 10 cm/s. Figure 9(a) shows the contour plot of the efficiency when the base doping N_a and the diffusion length L are varied. For $N_a = 1 \times 10^{18} \text{ cm}^{-3}$ and $L = 300 \mu\text{m}$ (equivalently, $\tau_{\text{neff}} = 0.13 \text{ ms}$ and $\tau_{\text{peff}} = 0.22 \text{ ms}$), the conversion efficiency η reaches about 30%. When Auger recombination is included, the optimum efficiency drops to about 28% [Fig. 9(b)].

In Fig. 9(b), we consider the Auger limited model where we vary the doping of the emitter and base to find the optimized doping level. In this model, increased doping leads to more Auger recombination and a shorter diffusion length. On the other hand, high doping is advantageous for achieving a high V_{OC} value. The trade-off between doping concentration and diffusion length leads to an optimum doping. Figure 9(b) shows that η reaches its maximum value of 27.9% for $N_d = 2 \times 10^{18} \text{ cm}^{-3}$ and $N_a = 2 \times 10^{17} \text{ cm}^{-3}$ when the junction is 100 nm below the top surface of the cell. Note that this is well beyond the current record efficiency of 26.3% [1,4].

Figure 10 shows the effect of the front and rear SRVs on the performance of the solar cell under different doping levels. Here again, we treat diffusion length as a variable independent of doping to accommodate possible lifetimes of the order of milliseconds, potentially achieved by advanced material processing technologies such as the hydrogenation of Si [44]. Figures 10(a), 10(c), and 10(e) correspond to the case when both $\text{SRV}_{\text{front}}$ and SRV_{rear} are varied (maintaining $\text{SRV}_{\text{rear}} = \text{SRV}_{\text{front}}$). Figures 10(b), 10(d), and 10(f) correspond to varying SRV_{rear} only,

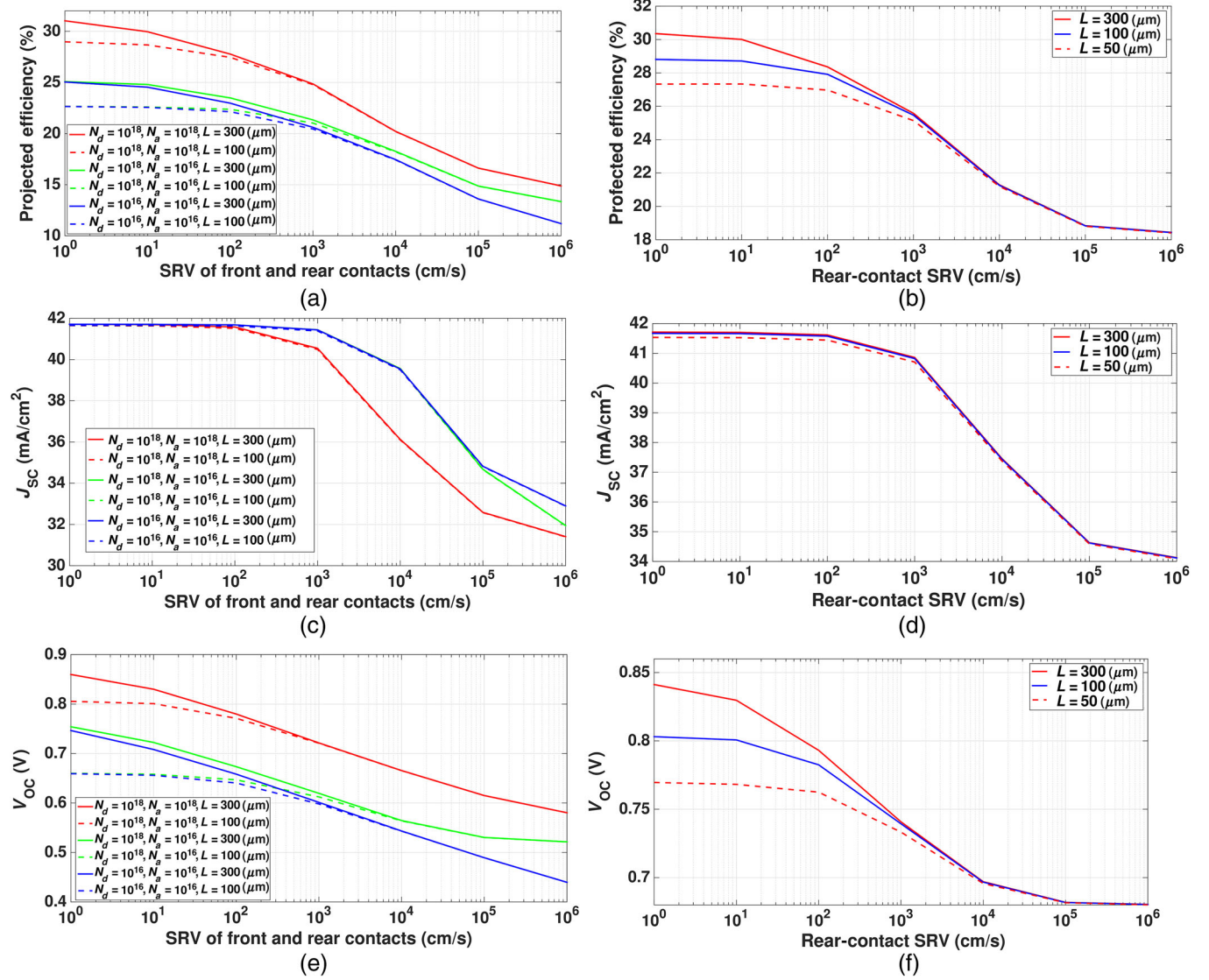


FIG. 10. Effect of SRV_{front} and SRV_{rear} on solar-cell performance. (a), (c), (e) correspond to a simultaneous variation of SRV_{front} and SRV_{rear} , (b), (d), (f) correspond to varying only SRV_{rear} keeping SRV_{front} fixed at 10 cm/s. The diffusion length is assumed to be doping independent. For the plots in the right column, we set $N_a = N_d = 10^{18}$ cm⁻³. The plots show that, over a SRV range of 1–10³ cm/s, V_{OC} drops off more strongly than J_{SC} .

keeping SRV_{front} fixed at 10 cm/s and doping levels for the base and emitter fixed at 10¹⁸ cm⁻³. Figures 10(a), 10(c), and 10(e) show that diffusion length becomes a decisive factor for low SRVs. For SRVs beyond 1000 cm/s, there is no difference between $L = 300$ μm and $L = 100$ μm. However, at $SRV_{\text{front}} = SRV_{\text{rear}} = 10$ cm/s, changing the diffusion length from 100 to 300 μm results in an approximately 2% increase in efficiency. Figures 10(c), 10(d), 10(e), and 10(f) show that J_{SC} remains relatively insensitive to the variation of the SRV below 10 cm/s and diffusion lengths longer than 50 μm. By contrast, for long diffusion lengths, V_{OC} falls off rapidly with the SRV. Furthermore, Fig. 10(b) shows that, with $N_a = N_d = 10^{18}$ cm⁻³ and $L = 50$ μm ($\tau_{\text{neff}} = 3.5$ μs and $\tau_{\text{peff}} = 6$ μs),

we can achieve above a 27% conversion efficiency for $SRV_{\text{front}} = SRV_{\text{rear}} = 10$ cm/s.

In general, moving the junction away from the top surface of the solar cell is detrimental to efficiency due to the increased distance that low-mobility, minority holes must diffuse to escape the region of high Auger recombination. For example, if the position of the p - n junction is moved from 100 to 170 nm below the top passivation-layer–Si interface while we maintain the optimum doping concentration, the projected efficiency of the cell drops to 27.82%. However, using a 170-nm Gaussian doping profile [Fig. 11(a)] for the emitter J - V characteristics [Fig. 11(b)] reveals a slightly improved FF, leading to a 28.05% conversion efficiency. The Gaussian doping profile for

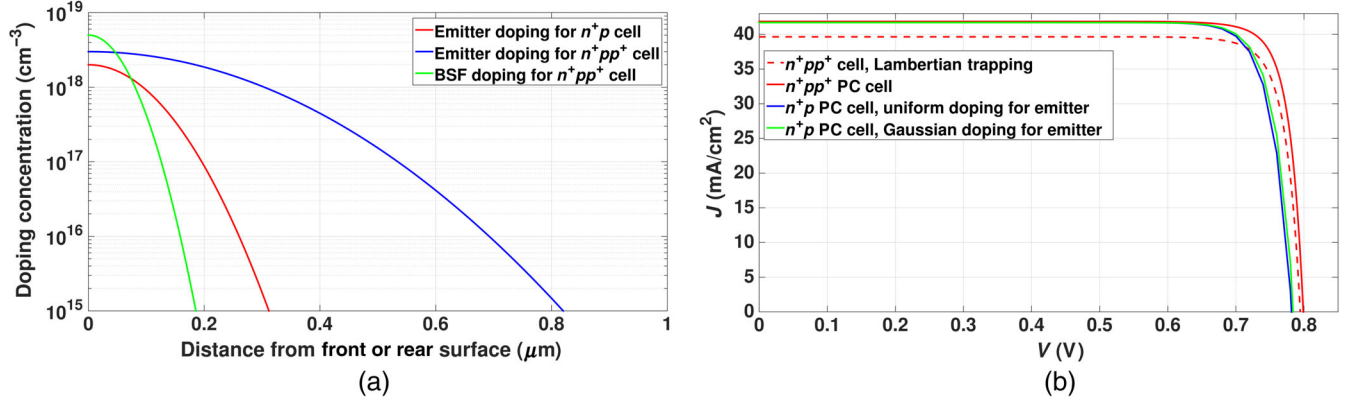


FIG. 11. (a) Gaussian doping profile for an n^+ emitter in an (n^+p) -type cell and the n^+ and p^+ regions in an (n^+pp^+) -type cell. (b) Comparison of J - V characteristics of an n^+p cell with uniform emitter doping ($\eta = 27.82\%$), an n^+p cell with Gaussian emitter doping ($\eta = 28.05\%$), and an n^+pp^+ cell ($\eta = 29.11\%$) with Gaussian doping for approximately 170-nm-thick n^+ and p^+ regions. For the n^+p cell, the junction is situated 170 nm below the top passivation-layer-Si interface. For the n^+pp^+ cell, the p region is uniformly doped with $N_a = 5 \times 10^{15} \text{ cm}^{-3}$. The n^+pp^+ cell exhibits $V_{OC} = 0.799 \text{ V}$. The red dashed curve corresponds to the J - V characteristics of an n^+pp^+ cell that employs perfect Lambertian light trapping ($J_{MAPD} = 39.65 \text{ mA/cm}^2$). Without slanted parabolic-pore PhC-assisted light trapping, the n^+pp^+ cell would have $\eta = 27.26\%$. All of the calculations take into account Richter's improved Auger model.

the emitter is given by $N = N_{f0} \exp(-z^2/2\sigma_f^2)$, where $N_{f0} = 2 \times 10^{18} \text{ cm}^{-3}$, $\sigma_f = 80 \text{ nm}$, and z denotes the distance from the passivation-layer-Si interface. The efficiency is further improved using Gaussian doping profiles (approximately 170 nm thick) for both the n^+ and p^+ regions, with relatively low, uniform doping ($N_a = 5 \times 10^{15} \text{ cm}^{-3}$) throughout the interior. For the front n^+ region, we choose $N_{f0} = 3 \times 10^{18} \text{ cm}^{-3}$ and $\sigma_f = 45 \text{ nm}$, whereas, for the rear p^+ region, we choose $N_{r0} = 5 \times 10^{18} \text{ cm}^{-3}$ and $\sigma_r = 45 \text{ nm}$ [Fig. 11(a)]. Figure 11(b) shows that the n^+pp^+ cell exhibits a 29.11% power conversion efficiency due to a significantly improved V_{OC} and FF. In order to highlight the improvement provided by PhC-assisted wave-interference-based light trapping, we show the J - V characteristics of the same 10- μm -thick n^+pp^+ cell assuming perfect Lambertian light trapping with a MAPD of 39.65 mA/cm². The hypothetical Lambertian n^+pp^+ cell provides only a 27.26%

conversion efficiency with $J_{SC} = 39.65 \text{ mA/cm}^2$, $V_{OC} = 0.7945 \text{ V}$, $\text{FF} = 86.55\%$. Our slanted parabolic-pore PhC cell offers nearly 2% more (additive) power conversion efficiency than the hypothetical cell constrained by the Lambertian limit.

Table I compares our proposed high-efficiency thin silicon solar cells with the 25%-efficient PERL cell and the record efficiency holding c -Si solar cell recently fabricated by Kaneka Corporation [5]. This comparison suggests that our PhC solar cells may outperform the thicker cells by achieving a higher V_{OC} through reduced bulk recombination. The transport results for our PhC cells in Table I are cross-checked using TCAD SENTAURUS [50] and Richter's improved Auger model [45].

V. PRACTICAL CONSIDERATIONS

In this section, we consider several real-world issues that could decrease the projected efficiency of our cell from

TABLE I. Comparison of the proposed PhC thin silicon solar cells using the Auger recombination model with the existing high-efficiency single-junction solar cells. For the n^+p and n^+pp^+ PhC solar cells, the p -type substrate is uniformly doped with $N_a = 2 \times 10^{17} \text{ cm}^{-3}$ and $5 \times 10^{15} \text{ cm}^{-3}$, respectively.

Cell type	Thickness (μm)	J_{SC} (mA/cm ²)	V_{OC} (V)	FF (%)	η (%)
Photonic crystal n^+p cell, junction at 100 nm, uniformly doped emitter	10	41.70	0.7836	85.49	27.94
Photonic crystal n^+p cell, junction at 170 nm, uniformly doped emitter	10	41.70	0.7817	85.35	27.82
Photonic crystal n^+p cell, junction at 170 nm, emitter with Gaussian doping profile	10	41.70	0.7839	85.80	28.05
Photonic crystal n^+pp^+ cell, 170-nm-thick n^+ and p^+ regions with Gaussian doping profile	10	41.72	0.7990	87.32	29.11
Kaneka Corporation	165	42.3	0.7440	83.80	26.30
PERL	400	42.7	0.7060	82.80	24.96

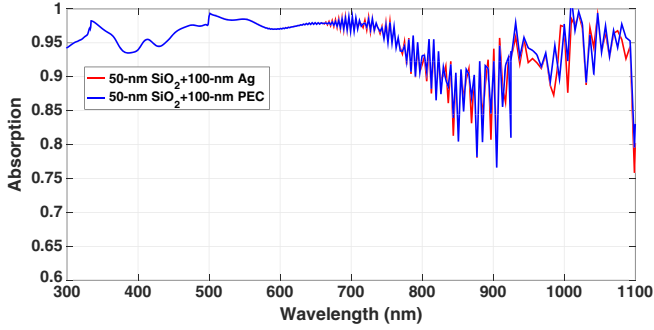


FIG. 12. Comparison of absorption spectra of optimized slanted parabolic-pore PhC with Ag and PEC backreflectors. The Ag backreflector causes a 0.04 mA/cm^2 drop in the MAPD compared to the PEC backreflector. Thus, the efficiency of the solar cell remains practically unaffected by the use of the Ag backreflector. This result is consistent with simulations carried out in Ref. [51], where it was shown that SiO_2 -Ag combination has more than 99% reflectivity compared to Ag alone (approximately 96% reflectivity).

over 29%. These issues include the use of lossy metals instead of a PEC for the rear contact and backreflector, power loss in the emitter region due to sheet resistance, and an increased surface recombination velocity. We do not explicitly consider shadowing loss of the front contacts given recent advances in broadband, wide-angle cloaked contacts [34–37], and IBCs [5,30–32].

Silver is a useful contact material due to its very low resistivity. As a backreflector, Ag sometimes yields nonideal reflectivity (of about 96%) [51], and the associated parasitic absorption can reduce the MAPD by $0.3\text{--}0.8 \text{ mA/cm}^2$ [12,18,52,53]. By contrast, we consider a combination of SiO_2 and Ag which has above 99% reflectivity [51]. Our SiO_2 PEC mimics the near-perfect reflectivity of a SiO_2 -Ag backreflector. To demonstrate this comparison, we implement the wavelength-dependent n and k (the real and imaginary parts of refractive index) of

Ag through an accurate fitting of experimental data [54] with the Drude critical points model [55]. Figure 12 compares the absorption spectra of the optimized slanted parabolic-pore PhC with SiO_2 -Ag and SiO_2 -PEC backreflectors in the absence of ARC. These absorption spectra correspond to 41.56 and 41.6 mA/cm^2 MAPDs, respectively.

We now consider the issue of sheet resistance in emitter-design optimization. Figure 13(a) shows the emitter optimization map with respect to the peak donor concentration N_{f0} and the emitter Gaussian width, neglecting sheet resistance. For a given σ_f value, as N_{f0} increases, the emitter field gradient increases, improving the collection of majority electrons while repelling the minority holes. However, a greater N_{f0} value increases Auger recombination. For a given σ_f value, N_{f0} exhibits an optimum balance between the Auger recombination and the front-surface field. As σ_f decreases, bulk recombination in the cell decreases. Near our bottom contact, we use a 170-nm -thick p^+ BSF with a Gaussian doping profile and the peak acceptor concentration $N_{r0} = 5 \times 10^{18} \text{ cm}^{-3}$. In Fig. 13(a), we find, for the top contact, optimum values of $N_{f0} = 3 \times 10^{18} \text{ cm}^{-3}$ and $\sigma_f = 45 \text{ nm}$ for a conversion efficiency of 29.1%. This value corresponds precisely to our choice of 170 nm overall emitter width for our 1D model of the n^+pp^+ cell.

In practice, emitter thickness must be large enough to prevent ion migration from the front contact to the shallow junction. Also, with a decreasing emitter width, the lateral component of the emitter current has to flow to the nearest contact finger through a narrower region. The resulting sheet resistance is a further source of power loss. The power loss (P_{loss}) in the emitter due to sheet resistance can be estimated as a fraction of the generated power P_{gen} [56]. The actual efficiency of a real-world solar cell is $\eta_{\text{actual}} = \eta(1 - P_{\text{loss}}/P_{\text{gen}})$. For concreteness, we consider

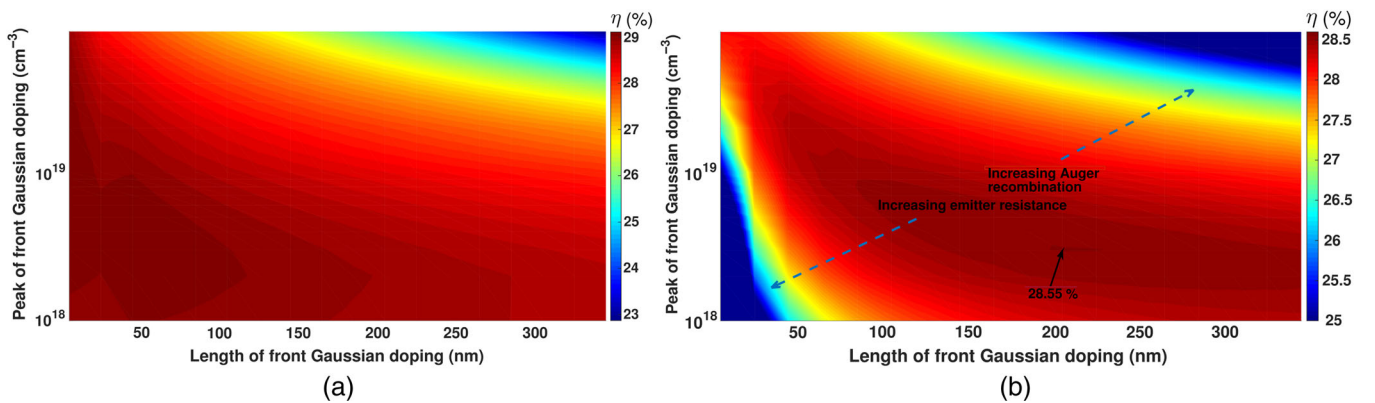


FIG. 13. Emitter optimizations of a slanted parabolic-pore PhC solar cell that (a) neglects power loss in the emitter and (b) includes power loss in the emitter. The finger spacing is assumed to be $800 \mu\text{m}$ (the same as for the 25% PERL cell [23]). Including sheet resistance, a maximum efficiency of 28.5% is obtained for $N_{f0} = 3 \times 10^{18} \text{ cm}^{-3}$ and $\sigma_f = 205 \text{ nm}$ (equivalent to an emitter width of 730 nm and a sheet resistance of $362 \Omega/\text{sq}$).

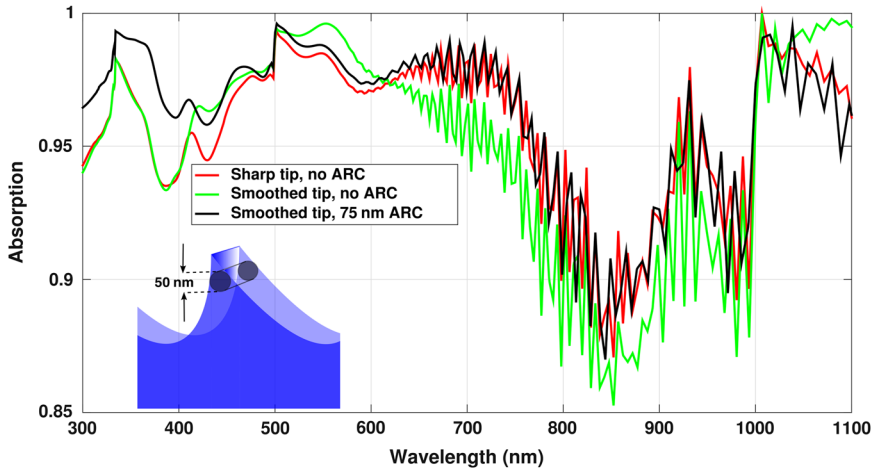


FIG. 14. Absorption spectra of an optimized slanted parabolic-pore PhC. Red curve, unperturbed (i.e., with a sharp tip) slanted parabolic-pore PhC (without ARC), corresponding to $J_{\text{MAPD}} = 41.6 \text{ mA/cm}^2$; green curve, PhC with a smoothed tip (without ARC), corresponding to $J_{\text{MAPD}} = 41.3 \text{ mA/cm}^2$; black curve, PhC with a smoothed tip and 75 nm of ARC, corresponding to $J_{\text{MAPD}} = 41.71 \text{ mA/cm}^2$. (Inset) The model used to simulate a smoothed tip.

a cell with finger spacing of $800 \mu\text{m}$ and a finger width of $20 \mu\text{m}$ as deployed in the 25%-efficient PERL cell [23] and a more recent tunnel oxide passivated contact (TOPCon) cell [57]. Feldmann *et al.* [57] showed that, for $800\text{-}\mu\text{m}$ finger spacing and a $20\text{-}\mu\text{m}$ low-resistivity Ag finger width, resistance loss in the finger is negligible. The sheet resistances corresponding to different N_{f0} and σ_f values are calculated using the PV Lighthouse sheet-resistance calculator [58]. The emitter optimization map including sheet resistance is shown in Fig. 13(b). As the emitter width decreases, the sheet resistance increases while the Auger recombination decreases, leading to a revised optimum emitter doping profile. A maximum efficiency of 28.55% is achieved for $N_{f0} = 3 \times 10^{18} \text{ cm}^{-3}$ and $\sigma_f = 205 \text{ nm}$ (equivalently, an emitter width of 730 nm). The sheet resistance at this optimum point is $362 \Omega/\text{sq}$. In this concrete example of upper-contact geometry with the emitter sheet resistance included, the projected efficiency drops only slightly from its previously estimated value of 29.11%.

Another source of unwanted recombination at the front surface of our cell is the sharp tip between two parabolic pores. These sharp protrusions can be smoothed out during the fabrication process with negligible loss in light trapping

and solar absorption. We model this smoothing out by replacing the knife edge with a 50-nm-diameter cylinder. Figure 14 shows that this rounded tip causes more reflection in the (625–1000)-nm spectral range, reducing the MAPD to 41.3 mA/cm^2 . However, the addition of a 75-nm nonconformal ARC on the rounded tips brings the MAPD up to 41.71 mA/cm^2 , just shy of the previously quoted optimum of 41.72 mA/cm^2 . This calculation shows that our PhC structure is robust to small variations in fabrication that, at the same time, remove unwanted recombination centers.

Finally, we consider the effect of increased front-contact SRV on the performance of our proposed cell. Experimental studies by Min *et al.* showed that front SRV ($\text{SRV}_{\text{front}}$) of SiN_x -passivated *c*-Si solar cells with industrial emitters may exceed 10^3 cm/s [27]. On the other hand, Kerr *et al.* showed that emitters passivated with an annealed thin oxide (SiO_2) has a lower $\text{SRV}_{\text{front}} \sim 200 \text{ cm/s}$ [59]. Also, the effective SRV_{rear} for passivated emitter rear contact (PERC) cells are approximately 15–20 cm/s [25,60]. Figure 15 shows the variation of efficiency with $\text{SRV}_{\text{front}}$ for a fixed $\text{SRV}_{\text{rear}} = 20 \text{ cm/s}$. At $\text{SRV}_{\text{front}} = 200 \text{ cm/s}$, the conversion efficiency of our cell is 28.25% (approximately 0.6% less than efficiency at $\text{SRV}_{\text{front}} = 10 \text{ cm/s}$). Overall, these

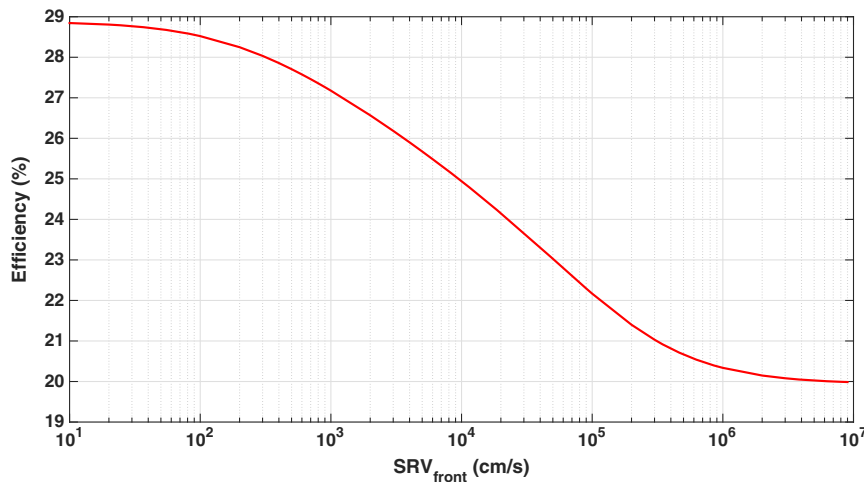


FIG. 15. Dependence of efficiency of an optimized slanted parabolic-pore PhC solar cell on $\text{SRV}_{\text{front}}$. SRV_{rear} is kept fixed at 20 cm/s .

real-world considerations yield a projected efficiency close to 28% when proper optimization is done.

VI. CONCLUSIONS

In summary, we show in this paper that, when using wave-interference-based light trapping, it is possible to absorb sunlight in the wavelength range of 300–1100 nm, in a 10- μm -thick crystalline silicon solar cell, corresponding to a photocurrent density of 41.7 mA/cm² out of a maximum available 43.5 mA/cm². In this parabolic-pore photonic crystal with a lattice constant of 1000 nm, we identify the important role of x - y symmetry breaking in absorbing near-infrared light through parallel-to-interface refraction into slow-light modes. The resulting solar absorption exceeds the Lambertian limit of 39.65 mA/cm².

It is likely that band-gap narrowing effects in crystalline silicon [61] would enable absorption of sunlight throughout the range of 300–1165 nm. In this case, the total available sunlight corresponds to a MAPD of 45.12 mA/cm². Our optimized slanted-pore structure reaches a MAPD of 43.3 mA/cm² instead of the 41.7 mA/cm² result found for the narrower spectral window. This additional MAPD might more than offset the slight decrease in V_{OC} and, possibly, lead to higher power conversion efficiency than our present estimates.

Our electronics model consists of a simple doping profile with (100–170)-nm n -type silicon at the top with a donor concentration of $2 \times 10^{18} \text{ cm}^{-3}$ and a large p -type silicon region below, with an acceptor concentration of $2 \times 10^{17} \text{ cm}^{-3}$. Using an Auger recombination model for the bulk, we find a power conversion efficiency of about 28% when the effective surface recombination velocities at the top and bottom are reduced to 10 cm/s. In this Auger model for bulk carrier recombination, the carrier diffusion length is fixed by the doping concentration. The combination of wave-interference-based light trapping in thin silicon and low surface recombination velocities offers a route to efficiencies above 29% within the Auger recombination model. This efficiency has been achieved using a more elaborate doping profile. For instance, bulk Auger recombination can be greatly reduced by lowering the doping concentration to $5 \times 10^{15} \text{ cm}^{-3}$ throughout most of the acceptor p region, but increasing the donor and acceptor doping to above 10^{18} cm^{-3} according to a Gaussian profile in a narrow 170-nm region near the top and bottom contacts. Such a profile allows the solar cell to maintain a high V_{OC} while, at the same time, reducing bulk recombination losses.

Finally, real-world effects, such as sheet-resistance and increased recombination velocity near the top contact, still yield a projected power conversion efficiency of about 28%. The consideration of sheet resistance allows us to identify optimum emitter design with Gaussian doping. A maximum conversion efficiency of 28.55% is achieved for

a peak emitter doping of $3 \times 10^{18} \text{ cm}^{-3}$ and 730-nm emitter thickness. This configuration provides the best balance between recombination loss in the emitter and power loss due to sheet resistance for a specific choice of upper-contact spacing. Overall, the parabolic-pore PhC with PERC architecture offers unprecedented power conversion efficiency, with only 10- μm c -Si. Other architectures worthy of study are SHJ-IBC and TOPCon cells. The TOPCon cells considered by Feldmann *et al.* [57] offer higher efficiency owing to an improved V_{OC} compared to a conventional passivated emitter, rear totally diffused cell. Also, single-heterojunction cells offer a higher V_{OC} due to the wider band gap of amorphous Si.

Our theoretical road map for light-trapping nanostructure design, doping profiles, and surface passivation offers a number of routes to thin silicon solar cells that surpass the power conversion efficiency of any single-junction silicon solar cell to date. It is hoped that these results will inspire experimental and fabrication efforts to realize the required structures.

ACKNOWLEDGMENTS

We are grateful to Professor S. Y. Lin and Dr. P. Kuang for the valuable discussions. This work was supported by the U.S. DOE-BES in a subcontract under Award No. DE-FG02-06ER46347.

-
- [1] National Renewable Energy Laboratory, Best research-cell efficiencies, <https://www.nrel.gov/pv/assets/images/efficiency-chart.png> (2016).
 - [2] W. Shockley and H. J. Queisser, Detailed balance limit of efficiency of p - n junction solar cells, *J. Appl. Phys.* **32**, 510 (1961).
 - [3] A. Richter, M. Hermle, and S. W. Glunz, Reassessment of the limiting efficiency for crystalline silicon solar cells, *IEEE J. Photovoltaics* **3**, 1184 (2013).
 - [4] M. A. Green, K. Emery, Y. Hishikawa, W. Warta, E. D. Dunlop, D. H. Levi, and A. W. Y. Ho-Baillie, Solar cell efficiency tables (version 49), *Prog. Photovoltaics* **25**, 3 (2017).
 - [5] K. Yoshikawa, H. Kawasaki, W. Yoshida, T. Irie, K. Konishi, K. Nakano, T. Uto, D. Adachi, M. Kanematsu, H. Uzu, and K. Yamamoto, Silicon heterojunction solar cell with interdigitated back contacts for a photoconversion efficiency over 26%, *Nat. Energy* **2**, 17032 (2017).
 - [6] S. Hargreaves, L. E. Black, D. Yan, and A. Cuevas, Modelling of silicon solar cells with up-to-date material parameters, *Energy Procedia* **38**, 66 (2013).
 - [7] S. Y. Herasimenka, W. J. Dauksher, and S. G. Bowden, >750 mV open circuit voltage measured on 50 μm thick silicon heterojunction solar cell, *Appl. Phys. Lett.* **103**, 053511 (2013).
 - [8] S. Yoshida, M. Hirai, Y. Abe, M. Konagai, and Y. Ichikawa, Single crystalline silicon solar cells with rib structure, *AIP Adv.* **7**, 025104 (2017).

- [9] S. John, Strong Localization of Photons in Certain Disordered Dielectric Superlattices, *Phys. Rev. Lett.* **58**, 2486 (1987).
- [10] E. Yablonovitch, Inhibited Spontaneous Emission in Solid-State Physics and Electronics, *Phys. Rev. Lett.* **58**, 2059 (1987).
- [11] G. Demsey and S. John, Solar energy trapping with modulated silicon nanowire photonic crystals, *J. Appl. Phys.* **112**, 074326 (2012).
- [12] S. Eyderman, S. John, and A. Deinega, Solar light trapping in slanted conical-pore photonic crystals: Beyond statistical ray trapping, *J. Appl. Phys.* **113**, 154315 (2013).
- [13] S. Eyderman, S. John, M. Hafez, S. S. Al-Ameer, T. S. Al-Harby, Y. Al-Hadeethi, and D. M. Bouwes, Light-trapping optimization in wet-etched silicon photonic crystal solar cells, *J. Appl. Phys.* **118**, 023103 (2015).
- [14] A. Chutinan and S. John, Light trapping and absorption optimization in certain thin-film photonic crystal architectures, *Phys. Rev. A* **78**, 023825 (2008).
- [15] T. Tiedje, E. Yablonovitch, G. Cody, and B. Brooks, Limiting efficiency of silicon solar cells, *IEEE Trans. Electron Devices* **31**, 711 (1984).
- [16] A. Mavrokefalos, S. E. Han, S. Yerci, M. S. Branham, and G. Chen, Efficient light trapping in inverted nanopyramid thin crystalline silicon membranes for solar cell applications, *Nano Lett.* **12**, 2792 (2012).
- [17] M. S. Branham, W. Hsu, S. Yerci, J. Loomis, S. V. Boriskina, B. R. Hoard, S. E. Han, and G. Chen, 15.7% efficient 10- μm -thick crystalline silicon solar cells using periodic nanostructures, *Adv. Mater.* **27**, 2182 (2015).
- [18] S. Foster and S. John, Light-trapping design for thin-film silicon-perovskite tandem solar cells, *J. Appl. Phys.* **120**, 103103 (2016).
- [19] P. Kuang, S. Eyderman, M. L. Hsieh, A. Post, S. John, and S. Y. Lin, Achieving an accurate surface profile of a photonic crystal for near-unity solar absorption in a super thin-film architecture, *ACS Nano* **10**, 6116 (2016).
- [20] A. Luque and A. Marti, Increasing the Efficiency of Ideal Solar Cells by Photon Induced Transitions at Intermediate Levels, *Phys. Rev. Lett.* **78**, 5014 (1997).
- [21] R. W. Peng, M. Mazzer, and K. W. J. Barnham, Efficiency enhancement of ideal photovoltaic solar cells by photonic excitations in multi-intermediate band structures, *Appl. Phys. Lett.* **83**, 770 (2003).
- [22] K. Q. Le and S. John, Synergistic plasmonic and photonic crystal light-trapping: Architectures for optical upconversion in thin-film solar cells, *Opt. Express* **22**, A1 (2014).
- [23] A. Wang, J. Zhao, and M. A. Green, 24% efficient silicon solar cells, *Appl. Phys. Lett.* **57**, 602 (1990).
- [24] M. A. Green, K. Emery, Y. Hishikawa, and W. Warta, Solar cell efficiency tables (version 37), *Prog. Photovoltaics* **19**, 84 (2011).
- [25] S. J. Robinson, S. R. Wenham, P. P. Altermatt, A. G. Aberle, G. Heiser, and M. A. Green, Recombination rate saturation mechanisms at oxidized surfaces of high-efficiency silicon solar cells, *J. Appl. Phys.* **78**, 4740 (1995).
- [26] P. Mahtani, K. R. Leong, B. Jovet, D. Yeghikyan, and N. P. Kherani, High quality amorphous-crystalline silicon heterostructure prepared by grid-biased remote radio-frequency plasma enhanced chemical vapor deposition, *J. Non-Cryst. Solids* **358**, 3396 (2012).
- [27] B. Min, H. Wagner, A. Dastgheib-Shirazi, A. Kimmerle, H. Kurz, and P. P. Altermatt, Heavily doped Si:P emitters of crystalline Si solar cells: Recombination due to phosphorus precipitation, *Phys. Status Solidi RRL* **8**, 680 (2014).
- [28] R. S. Bonilla, B. Hoex, P. Hamer, and P. R. Wilshaw, Dielectric surface passivation for silicon solar cells: A review, *Phys. Status Solidi A* **214**, 1700293 (2017).
- [29] A. W. Blakers, Shading losses of solar-cell metal grids, *J. Appl. Phys.* **71**, 5237 (1992).
- [30] E. V. Kerschaver and G. Beaucarne, Back-contact solar cells: A review, *Prog. Photovoltaics* **14**, 107 (2006).
- [31] C. Battaglia, A. Cuevas, and S. D. Wolf, High-efficiency crystalline silicon solar cells: Status and perspectives, *Energy Environ. Sci.* **9**, 1552 (2016).
- [32] M. K. Mat Desa, S. Sapeai, A. W. Azhari, K. Sopian, M. Y. Sulaiman, N. Amin, and S. H. Zaidi, Silicon back contact solar cell configuration: A pathway towards higher efficiency, *Renewable Sustainable Energy Rev.* **60**, 1516 (2016).
- [33] S. Bhattacharya and S. John (to be published).
- [34] M. F. Schumann, S. Wiesendanger, J. C. Goldschmidt, B. Blasi, K. Bittkau, U. W. Paetzold, A. Sprafke, R. B. Wehrspohn, C. Rockstuhl, and M. Wegner, Cloaked contact grids on solar cells by coordinate transformations: Designs and prototypes, *Optica* **2**, 850 (2015).
- [35] M. Langenhorst, M. F. Schumann, R. Schmager, J. Lehr, U. Lemmer, M. Wegener, B. Richards, and U. W. Paetzold, in *Proceedings of Optical Nanostructures and Advanced Materials for Photovoltaics, Boulder, 2017* (Optical Society of America, Washington, DC, 2017), p. PW2A.3.
- [36] M. F. Schumann, M. Langenhorst, M. Smeets, K. Ding, U. W. Paetzold, and M. Wegener, All-angle invisibility cloaking of contact fingers on solar cells by refractive free-form surfaces, *Adv. Opt. Mater.* **5**, 1700164 (2017).
- [37] E. S. Roman, A. Vitrey, J. Buencuerpo, I. Prieto, J. M. Llorens, A. Garcia-Martin, B. Alen, A. Chaudhuri, A. Neumann, S. R. J. Brueck, and J. M. Ripalda, Cloaking of solar cell contacts at the onset of Rayleigh scattering, *Sci. Rep.* **6**, 28669 (2016).
- [38] Z. R. Chowdhury, K. Cho, and N. P. Kherani, High-quality surface passivation of silicon using native oxide and silicon nitride layers, *Appl. Phys. Lett.* **101**, 021601 (2012).
- [39] S. Calnan, O. Gabriel, I. Rothert, M. Werth, S. Ring, B. Stannowski, and R. Schlattmann, Influence of chemical composition and structure in silicon dielectric materials on passivation of thin crystalline silicon on glass, *ACS Appl. Mater. Interfaces* **7**, 19282 (2015).
- [40] I. Valuev, A. Deinega, A. Knizhnik, and B. Potapkin, in *Computational Science and Its Applications—ICCSA 2007*, edited by O. Gervasi and M. L. Gavrilova, *Lecture Notes in Computer Science*, Vol. 4707 (Springer, New York, 2007), p. 213.
- [41] A. Deinega and S. John, Finite difference discretization of semiconductor drift-diffusion equations for nanowire solar cells, *Comput. Phys. Commun.* **183**, 2128 (2012).
- [42] M. A. Green, Self-consistent optical parameters of intrinsic silicon at 300 K including temperature coefficients, *Sol. Energy Mater. Sol. Cells* **92**, 1305 (2008).

- [43] G. Masetti, M. Severi, and S. Solmi, Modeling of carrier mobility against carrier concentration in arsenic-, phosphorus-, and boron-doped silicon, *IEEE Trans. Electron Devices* **30**, 764 (1983).
- [44] B. J. Hallam, P. G. Hamer, S. R. Wenham, M. D. Abbott, A. Sugianto, A. M. Wenham, C. E. Chan, G. Q. Xu, J. Kraiem, J. Degoulange, and R. Einhaus, Advanced bulk defect passivation for silicon solar cells, *IEEE J. Photovoltaics* **4**, 88 (2014).
- [45] A. Richter, S. W. Glunz, F. Werner, J. Schmidt, and A. Cuevas, Improved quantitative description of Auger recombination in crystalline silicon, *Phys. Rev. B* **86**, 165202 (2012).
- [46] T. Luder, G. Hahn, and B. Terheiden, Passivation of Si wafers by ALD- Al_2O_3 films with different surface conditioning, *Energy Procedia* **8**, 660 (2011).
- [47] J. Benick, A. Richter, M. Hermle, and S. W. Glunz, Thermal stability of the Al_2O_3 passivation on *p*-type silicon surfaces for solar cell applications, *Phys. Status Solidi RRL* **3**, 233 (2009).
- [48] M. J. Kerr and A. Cuevas, General parameterization of Auger recombination in crystalline silicon, *J. Appl. Phys.* **91**, 2473 (2002).
- [49] A. Luque and I. Tobias, Perimeter recombination in planar solar cells, *J. Appl. Phys.* **73**, 4042 (1993).
- [50] Synopsys, TCAD Sentaurus, release M-2016.12, 2016.
- [51] H. Cui, P. R. Campbell, and M. A. Green, Optimisation of the back surface reflector for textured polycrystalline Si thin film solar cells, *Energy Procedia* **33**, 118 (2013).
- [52] S. Eyderman, A. Deinega, and S. John, Near perfect solar absorption in ultra-thin-film GaAs photonic crystals, *J. Mater. Chem. A* **2**, 761 (2014).
- [53] Z. C. Holman, M. Filipic, B. Lipovsek, S. De Wolf, F. Smole, M. Topic, and C. Ballif, Parasitic absorption in the rear reflector of a silicon solar cell: Simulation and measurement of the sub-bandgap reflectance for common dielectric/metal reflectors, *Sol. Energy Mater. Sol. Cells* **120**, 426 (2014).
- [54] P. B. Johnson and R. W. Christy, Optical constants of the noble metals, *Phys. Rev. B* **6**, 4370 (1972).
- [55] A. Vial, T. Laroche, M. Dridi, and L. L. Cunff, A new model of dispersion for metals leading to a more accurate modeling of plasmonic structures using the FDTD method, *Appl. Phys. A* **103**, 849 (2011).
- [56] See <http://www.pveducation.org/pvcdrom/design/emitter-resistance>.
- [57] F. Feldmann, M. Bivour, C. Reichel, M. Hermle, and S. W. Glunz, Passivated rear contacts for high-efficiency *n*-type Si solar cells providing high interface passivation quality and excellent transport characteristics, *Sol. Energy Mater. Sol. Cells* **120**, 270 (2014).
- [58] PV Lighthouse, Sheet-resistance calculator, <https://www2.pvlighthouse.com.au/calculators/Sheet%20resistance%20calculator/Sheet%20resistance%20calculator.aspx>.
- [59] M. J. Kerr, J. Schmidt, A. Cuevas, and J. H. Bultman, Surface recombination velocity of phosphorus-diffused silicon solar cell emitters passivated with plasma enhanced chemical vapor deposited silicon nitride and thermal silicon oxide, *J. Appl. Phys.* **89**, 3821 (2001).
- [60] M. Muller *et al.*, Loss analysis of 22% efficient industrial PERC solar cells, *Energy Procedia* **124**, 131 (2017).
- [61] A. Schenk, Finite-temperature full random-phase approximation model of band gap narrowing for silicon device simulation, *J. Appl. Phys.* **84**, 3684 (1998).